

# Refined beam elements with only displacement variables and plate/shell capabilities

Erasmus Carrera · Marco Petrolo

**Abstract** This paper proposes a refined beam formulation with displacement variables only. Lagrange-type polynomials, in fact, are used to interpolate the displacement field over the beam cross-section. Three- (L3), four- (L4), and nine-point (L9) polynomials are considered which lead to linear, quasi-linear (bilinear), and quadratic displacement field approximations over the beam cross-section. Finite elements are obtained by employing the principle of virtual displacements in conjunction with the Unified Formulation (UF). With UF application the finite element matrices and vectors are expressed in terms of fundamental nuclei whose forms do not depend on the assumptions made (L3, L4, or L9). Additional refined beam models are implemented by introducing further discretizations over the beam cross-section in terms of the implemented L3, L4, and L9 elements. A number of numerical problems have been solved and compared with results given by classical beam theories (Euler-Bernoulli and Timoshenko), refined beam theories based on the use of Taylor-type expansions in the neighborhood of the beam axis, and solid element models from commercial codes. Poisson locking correction is analyzed. Appli-

cations to compact, thin-walled open/closed sections are discussed. The investigation conducted shows that: (1) the proposed formulation is very suitable to increase accuracy when localized effects have to be detected; (2) it leads to shell-like results in case of thin-walled closed cross-section analysis as well as in open cross-section analysis; (3) it allows us to modify the boundary conditions over the cross-section easily by introducing localized constraints; (4) it allows us to introduce geometrical boundary conditions along the beam axis which lead to plate/shell-like cases.

**Keywords** Finite element method · Higher-order beam · Shell-like capabilities · Carrera unified formulation

## 1 Introduction

Beam theories are important tools for structural analysts. Interest in beam models is mainly due to their simplicity and their low computational costs when compared to 2D (plate/shell) or 3D (solid) models. The use of a beam model is of particular interest with slender bodies such as aircraft wings, helicopter rotor blades, and slender bridges. The classical and best-known beam theories are those by Euler [16] and hereinafter referred as EBBM, and Timoshenko [30, 31] and hereinafter referred as TBM. The former does not account for transverse shear deformations. The latter foresees a uniform shear distribution along the

---

E. Carrera (✉) · M. Petrolo  
Department of Aeronautic and Space Engineering,  
Politecnico di Torino, Corso Duca degli Abruzzi 24,  
10129 Torino, Italy  
e-mail: erasmus.carrera@polito.it

M. Petrolo  
e-mail: marco.petrolo@polito.it

cross-section of the beam. These models work properly when slender compact homogeneous structures are considered in bending. Conversely, the analysis of deep, thin-walled, open beams requires more sophisticated methods, see [22]. Higher-order beam theories that enhance the displacement fields of EBBM and TBM can be developed to overcome these limits.

Several refined beam models can be found in open literature. Attention is herein given to works which are mainly devoted to the analysis of isotropic, thin-walled, and open cross-section beams. A comprehensive review of beam (including plate) theories for vibration, wave propagations, buckling and post-buckling was presented by Kapania and Raciti [20, 21]. An overview of existing beam finite elements was made by Reddy [25], where beam elements based on classical and higher-order theories were described, and the problems of shear locking and locking-free beam elements were discussed. Vinayak et al. [33] used a higher-order beam element based on the Lo-Christensen-Wu theory to study isotropic and composite, thin and deep compact beams, where axial and transverse displacements were modeled via cubic and parabolic expansions, respectively. Several works related to the shear correction factor evaluation were presented by Gruttmann et al. [18], Gruttmann and Wagner [17], and Wagner and Gruttmann [34]. Here, several structural problems were addressed: torsional and flexural shearing stresses in prismatic beams, arbitrary shaped cross-sections, wide and thin-walled structures, and the influence of Poisson's ratio on the shear correction factor was highlighted. A distortional theory for thin-walled beams was proposed by Jönsson [19], where the distortional displacement mode was embedded in the classical kinematic assumptions of Vlasov theory, and the role of cross-section distortion was investigated for different open and closed cross-sections undergoing static loads. Petrolito [24] and Eisenberger [13] dealt with the exact stiffness matrix analysis of a high-order beam element: the refined displacement field was based on a cubic variation of the axial displacement over the cross-section of the beam whereas the lateral displacement was kept constant, and comparisons with classical models were made, while the importance of higher order terms in case of short beams was underlined. Works by Dinis et al. [12] and Silvestre [29] dealt with the buckling analysis of thin walled open/closed cross-section beams: the Generalized Beam Theory

(GBT) was used to implement beam theories accounting for the in-plane cross-section deformations, and shell-type results were obtained by using appropriate cross-section shape functions describing the beam displacement field; the choice of those functions depends on the geometry of the considered structures. GBT was also used by Rendek and Baláz [27], for the static analysis of thin walled beams and comparisons with experimental results. El Fatmi [14, 15] proposed a beam theory with a non-uniform warping distribution. He adopted a kinematic model that keeps the cross-section shape constant; warping effects were investigated on compact and hollow beams with closed and open cross-sections, and particular attention was given to the analysis of shear and axial stresses. The proposed refined theory proved useful especially with short open cross-section beams. Another interesting work dealing with non-uniform warping distributions was presented by Sadé [28]; a detailed overview of the warping problem was given, and static and buckling analyses were performed. A different approach to refine a structural model is based on the asymptotic method where a characteristic parameter (e.g. the cross-section thickness for a beam) is exploited to build an asymptotic series, and those terms which exhibit the same order of magnitude as the parameter when it vanishes are retained. Significant examples of asymptotic built beam models were given by Yu et al. [36] and Yu and Hodges [35].

The above works show a clear interest in investigating refined beam theories. The present work falls in the framework of the Carrera Unified Formulation, CUF, which has been developed during the last decade by the first author and his co-workers. CUF was initially devoted to the development of refined plate and shell theories, see [2, 3]. Recently, it has been extended to beam modeling by Carrera and Giunta [6]. CUF is a hierarchical formulation which considers the order of the theory as an input of the analysis. This permits us to deal with a wide variety of problems with no need of ad hoc formulations. Non-classical effects (e.g. warping, in-plane deformations, shear effects, bending-torsion coupling) are accounted for by opportunely increasing the order of the adopted model. Finite element formulation is adopted to deal with arbitrary geometries, boundary conditions, and loadings. Previous works have been based on the use of Taylor type polynomials to define the displacement field above the beam cross-section; each field consists of

a direct extension to higher-order expansions of the Timoshenko beam theory. Static analyses, see [8, 11], showed the strength of CUF in dealing with warping, in-plane deformations, and shear effects. Free vibration analyses, see [9, 10], underlined the possibility of detecting shell-like vibration modes by means of refined beam theories with no need of more cumbersome 2D or 3D models. An effectiveness analysis by Car-rera and Petrolo [7] was also conducted to highlight the role of each higher-order term in given structural problems.

The use of Taylor-type expansions has some intrinsic limitations: the introduced variables have a mathematical meaning (derivatives at the beam axes); higher order terms cannot have a local meaning, they can have cross-section properties only; the extension to large rotation formulation could experience difficulties. To overcome these problems, this work proposes new beam theories whose cross-section displacement field is described by Lagrange-type polynomials. The choice of this kind of expansion functions leads us to have displacement variables only. This aspect is of particular interest because:

1. each variable has a precise physical meaning (the problem unknowns are only translational displacements);
2. unknown variables can be put in fixed zones (sub-domains) of the cross-section area (e.g. close to loadings);
3. geometrical boundary conditions can be applied in sub-domains of the cross-section (and not only to the whole cross-section);
4. geometrical boundary conditions can also be applied along the beam-axis;
5. cross-sections can be divided into further beam sections and easily assembled since the displacements at each boundary are used as problem unknowns;
6. the extension to geometrically non-linear problems appears more suitable than in the case of Taylor-type higher-order theories.

Three- (L3), four- (L4), and nine-point (L9) polynomials are considered in the framework of CUF; this leads to linear, quasi-linear (bilinear), and quadratic displacement field approximations over the beam cross-section. More refined beam models are implemented by introducing further discretizations over the beam cross-section in terms of implemented elements. A number of significant problems are treated. Compact, thin-walled, open cross-section, and shell-like

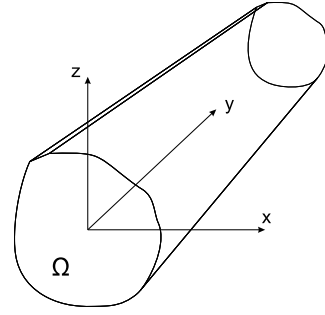


Fig. 1 Coordinate frame of the beam model

structures are analyzed. Homogenous isotropic models are used. The possibilities of dealing with localized loadings and to treat in a ‘new manner’ the geometrical boundary conditions are shown.

The paper is organized as follows: brief descriptions of the adopted beam theories and the finite element formulation are furnished in Sects. 2 and 3; structural problems addressed, together with results and discussion, are provided in Sect. 4. The main conclusions are then outlined in Sect. 5.

## 2 Preliminaries

The adopted coordinate frame is presented in Fig. 1. The beam boundaries over  $y$  are  $0 \leq y \leq L$ . The displacement vector is:

$$\mathbf{u}(x, y, z) = \{u_x \ u_y \ u_z\}^T \quad (1)$$

The superscript “ $T$ ” represents the transposition operator. Stress,  $\boldsymbol{\sigma}$ , and strain,  $\boldsymbol{\epsilon}$ , components are grouped as follows:

$$\begin{aligned} \boldsymbol{\sigma}_p &= \{\sigma_{zz} \ \sigma_{xx} \ \sigma_{zx}\}^T, & \boldsymbol{\epsilon}_p &= \{\epsilon_{zz} \ \epsilon_{xx} \ \epsilon_{zx}\}^T \\ \boldsymbol{\sigma}_n &= \{\sigma_{zy} \ \sigma_{xy} \ \sigma_{yy}\}^T, & \boldsymbol{\epsilon}_n &= \{\epsilon_{zy} \ \epsilon_{xy} \ \epsilon_{yy}\}^T \end{aligned} \quad (2)$$

The subscript “ $n$ ” stands for terms lying on the cross-section, while “ $p$ ” stands for terms lying on planes which are orthogonal to  $\Omega$ . Linear strain-displacement relations are used:

$$\begin{aligned} \boldsymbol{\epsilon}_p &= \mathbf{D}_p \mathbf{u} \\ \boldsymbol{\epsilon}_n &= \mathbf{D}_n \mathbf{u} = (\mathbf{D}_{n\Omega} + \mathbf{D}_{ny}) \mathbf{u} \end{aligned} \quad (3)$$

with:

$$\mathbf{D}_p = \begin{bmatrix} 0 & 0 & \frac{\partial}{\partial z} \\ \frac{\partial}{\partial x} & 0 & 0 \\ \frac{\partial}{\partial z} & 0 & \frac{\partial}{\partial x} \end{bmatrix}, \quad \mathbf{D}_{n\Omega} = \begin{bmatrix} 0 & 0 & 0 \\ 0 & \frac{\partial}{\partial x} & 0 \\ 0 & \frac{\partial}{\partial z} & 0 \end{bmatrix} \quad (4)$$

$$\mathbf{D}_{ny} = \begin{bmatrix} 0 & \frac{\partial}{\partial y} & 0 \\ \frac{\partial}{\partial y} & 0 & 0 \\ 0 & 0 & \frac{\partial}{\partial y} \end{bmatrix}$$

The Hooke law is exploited:

$$\boldsymbol{\sigma} = \mathbf{C}\boldsymbol{\epsilon} \quad (5)$$

According to (2), the previous equation becomes:

$$\begin{aligned} \boldsymbol{\sigma}_p &= \tilde{\mathbf{C}}_{pp}\boldsymbol{\epsilon}_p + \tilde{\mathbf{C}}_{pn}\boldsymbol{\epsilon}_n \\ \boldsymbol{\sigma}_n &= \tilde{\mathbf{C}}_{np}\boldsymbol{\epsilon}_p + \tilde{\mathbf{C}}_{nn}\boldsymbol{\epsilon}_n \end{aligned} \quad (6)$$

In the case of isotropic material the matrices  $\tilde{\mathbf{C}}_{pp}$ ,  $\tilde{\mathbf{C}}_{nn}$ ,  $\tilde{\mathbf{C}}_{pn}$ , and  $\tilde{\mathbf{C}}_{np}$  are:

$$\begin{aligned} \tilde{\mathbf{C}}_{pp} &= \begin{bmatrix} \tilde{C}_{11} & \tilde{C}_{12} & 0 \\ \tilde{C}_{12} & \tilde{C}_{22} & 0 \\ 0 & 0 & \tilde{C}_{66} \end{bmatrix} \\ \tilde{\mathbf{C}}_{nn} &= \begin{bmatrix} \tilde{C}_{55} & 0 & 0 \\ 0 & \tilde{C}_{44} & 0 \\ 0 & 0 & \tilde{C}_{33} \end{bmatrix} \\ \tilde{\mathbf{C}}_{pn} &= \tilde{\mathbf{C}}_{np}^T = \begin{bmatrix} 0 & 0 & \tilde{C}_{13} \\ 0 & 0 & \tilde{C}_{23} \\ 0 & 0 & 0 \end{bmatrix} \end{aligned} \quad (7)$$

For the sake of brevity, the dependence of coefficients  $[\tilde{C}]_{ij}$  versus Young's modulus and Poisson's ratio is not reported here. It can be found in the books by Tsai [32] or Reddy [26].

### 3 Unified FE formulation

In the framework of the Carrera Unified Formulation (CUF), the displacement field is the expansion of generic functions,  $F_\tau$ :

$$\mathbf{u} = F_\tau \mathbf{u}_\tau, \quad \tau = 1, 2, \dots, M \quad (8)$$

where  $F_\tau$  vary above the cross-section.  $\mathbf{u}_\tau$  is the displacement vector and  $M$  stands for the number of

**Table 1** L3 cross-section element point natural coordinates

Point	$r_\tau$	$s_\tau$
1	0	0
2	1	0
3	0	1

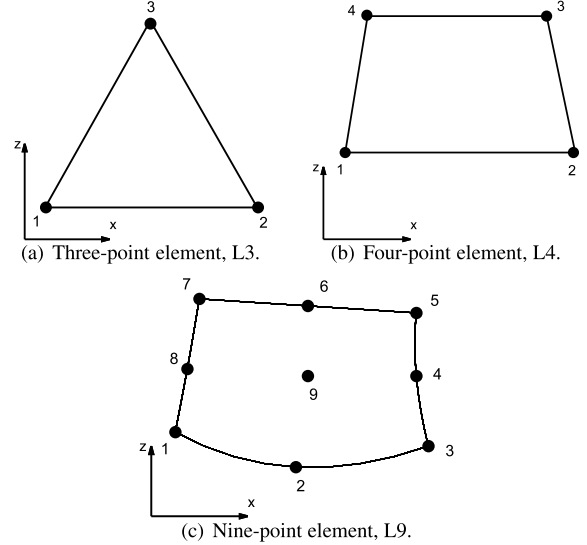


**Fig. 2** Cross-section elements in actual geometry

terms of the expansion. According to the Einstein notation, the repeated subscript,  $\tau$ , indicates summation. Taylor-type expansions have been exploited in previous works by Carrera and Giunta [6], Carrera and Petrolo [7], Carrera et al. [8–11]. The Euler-Bernoulli (EBBM) and Timoshenko (TBM) classical theories are derived from the linear Taylor-type expansion. Lagrange polynomials are herein used to describe the cross-section displacement field. Three-, L3, four-, L4, and nine-point, L9, polynomials are adopted. L3 polynomials are defined on a triangular domain which is identified by three points. These points define the element that is used to model the displacement field above the cross-section. Similarly, L4 and L9 cross-section elements are defined on quadrilateral domains. The isoparametric formulation is exploited. In the case of the L3 element, the interpolation functions are given by [23]:

$$F_1 = 1 - r - s, \quad F_2 = r, \quad F_3 = s \quad (9)$$

**Table 2** L4 cross-section element point natural coordinates

Point	$r_\tau$	$s_\tau$
1	-1	-1
2	1	-1
3	1	1
4	-1	1

**Table 3** L9 cross-section element point natural coordinates

Point	$r_\tau$	$s_\tau$
1	-1	-1
2	0	-1
3	1	-1
4	1	0
5	1	1
6	0	1
7	-1	1
8	-1	0
9	0	0

where  $r$  and  $s$  belong to the triangular domain defined by the points in Table 1. Figure 2a shows the point locations in actual coordinates. The L4 element interpolation functions are given by:

$$F_\tau = \frac{1}{4}(1 + rr_\tau)(1 + ss_\tau), \quad \tau = 1, 2, 3, 4 \quad (10)$$

where  $r$  and  $s$  vary from  $-1$  to  $+1$ . Figure 2b shows the point locations and Table 2 reports the point natural coordinates. In the case of a L9 element the interpolation functions are given by:

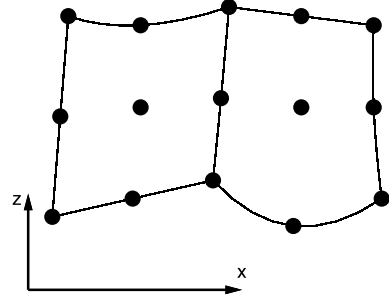
$$F_\tau = \frac{1}{4}(r^2 + rr_\tau)(s^2 + ss_\tau), \quad \tau = 1, 3, 5, 7$$

$$F_\tau = \frac{1}{2}s_\tau^2(s^2 - ss_\tau)(1 - r^2) + \frac{1}{2}r_\tau^2(r^2 - rr_\tau)(1 - s^2) \quad (11)$$

$$\tau = 2, 4, 6, 8$$

$$F_\tau = (1 - r^2)(1 - s^2), \quad \tau = 9$$

where  $r$  and  $s$  from  $-1$  to  $+1$ . Figure 2c shows the point locations and Table 3 reports the point natural coordinates. The displacement field given by an L4 element is:

**Fig. 3** Two assembled L9 elements

$$\begin{aligned} u_x &= F_1 u_{x_1} + F_2 u_{x_2} + F_3 u_{x_3} + F_4 u_{x_4} \\ u_y &= F_1 u_{y_1} + F_2 u_{y_2} + F_3 u_{y_3} + F_4 u_{y_4} \\ u_z &= F_1 u_{z_1} + F_2 u_{z_2} + F_3 u_{z_3} + F_4 u_{z_4} \end{aligned} \quad (12)$$

where  $u_{x_1}, \dots, u_{z_4}$  are the displacement variables of the problem and they represent the translational displacement components of each of the four points of the L4 element. The cross-section can be discretized by means of several L-elements. Figure 3 shows the assembly of 2 L9 which share a common edge and three points.

The discretization along the beam axis is conducted via a classical finite element approach. The displacement vector is given by:

$$\mathbf{u} = N_i F_\tau \mathbf{q}_{\tau i} \quad (13)$$

where  $N_i$  stands for the shape functions and  $\mathbf{q}_{\tau i}$  for the nodal displacement vector:

$$\mathbf{q}_{\tau i} = \{ q_{u_{x_{\tau i}}} \quad q_{u_{y_{\tau i}}} \quad q_{u_{z_{\tau i}}} \}^T \quad (14)$$

For the sake of brevity, the shape functions are not reported here. They can be found in many books, for instance in Bathe [1]. Elements with four nodes (B4) are herein formulated, that is, a cubic approximation along the  $y$  axis is adopted. It has to be highlighted that the adopted cross-section displacement field model defines the beam theory. It is therefore possible to deal with linear (L3), bilinear (L4), and quadratic (L9) beam theories. Further refinements can be obtained by adding cross-section elements, in this case the beam model will be defined by the number of cross-section elements used. The choice of the cross-section discretization (i.e. the choice of the type, the number and the distribution of cross-section elements) is completely independent of the choice of the beam finite element to be used along the beam axis.

The present formulation has to be considered as an 1D model since the unknowns of the problem, i.e. the nodal unknowns, vary along the beam axis whereas the displacement field of the beam is axiomatically modeled above the cross-section domain. The introduction of the Lagrange-like discretization above the cross-section allows us to deal with locally refinable 1D models having only displacement variables. This modeling choice represents the novelty of the present work since Taylor-like polynomials were exploited previously above the cross-section domain.

The stiffness matrix of the elements and the external loadings, which are consistent with the model, are obtained via the Principle of Virtual Displacements:

$$\delta L_{int} = \int_V (\delta \epsilon_p^T \sigma_p + \delta \epsilon_n^T \sigma_n) dV = \delta L_{ext} \quad (15)$$

where  $L_{int}$  stands for the strain energy, and  $L_{ext}$  is the work of the external loadings.  $\delta$  stands for the virtual variation. The virtual variation of the strain energy is rewritten using (3), (6) and (13):

$$\delta L_{int} = \delta \mathbf{q}_{\tau i}^T \mathbf{K}^{ij\tau s} \mathbf{q}_{sj} \quad (16)$$

where  $\mathbf{K}^{ij\tau s}$  is the stiffness matrix in the form of the fundamental nucleus. Its components are:

$$K_{xx}^{ij\tau s} = \tilde{C}_{22} \int_{\Omega} F_{\tau,x} F_{s,x} d\Omega \int_l N_i N_j dy$$

$$+ \tilde{C}_{66} \int_{\Omega} F_{\tau,z} F_{s,z} d\Omega \int_l N_i N_j dy$$

$$+ \tilde{C}_{44} \int_{\Omega} F_{\tau} F_s d\Omega \int_l N_{i,y} N_{j,y} dy$$

$$K_{xy}^{ij\tau s} = \tilde{C}_{23} \int_{\Omega} F_{\tau,x} F_s d\Omega \int_l N_i N_{j,y} dy$$

$$+ \tilde{C}_{44} \int_{\Omega} F_{\tau} F_{s,x} d\Omega \int_l N_{i,y} N_j dy$$

$$K_{xz}^{ij\tau s} = \tilde{C}_{12} \int_{\Omega} F_{\tau,x} F_{s,z} d\Omega \int_l N_i N_j dy$$

$$+ \tilde{C}_{66} \int_{\Omega} F_{\tau,z} F_{s,x} d\Omega \int_l N_i N_j dy$$

$$K_{yx}^{ij\tau s} = \tilde{C}_{44} \int_{\Omega} F_{\tau,x} F_s d\Omega \int_l N_i N_{j,y} dy$$

$$+ \tilde{C}_{23} \int_{\Omega} F_{\tau} F_{s,x} d\Omega \int_l N_{i,y} N_j dy$$

$$K_{yy}^{ij\tau s} = \tilde{C}_{55} \int_{\Omega} F_{\tau,z} F_{s,z} d\Omega \int_l N_i N_j dy$$

$$+ \tilde{C}_{44} \int_{\Omega} F_{\tau,x} F_{s,x} d\Omega \int_l N_i N_j dy \quad (17)$$

$$+ \tilde{C}_{33} \int_{\Omega} F_{\tau} F_s d\Omega \int_l N_{i,y} N_{j,y} dy$$

$$K_{yz}^{ij\tau s} = \tilde{C}_{55} \int_{\Omega} F_{\tau,z} F_s d\Omega \int_l N_i N_{j,y} dy$$

$$+ \tilde{C}_{13} \int_{\Omega} F_{\tau} F_{s,z} d\Omega \int_l N_{i,y} N_j dy$$

$$K_{zx}^{ij\tau s} = \tilde{C}_{12} \int_{\Omega} F_{\tau,z} F_{s,x} d\Omega \int_l N_i N_j dy$$

$$+ \tilde{C}_{66} \int_{\Omega} F_{\tau,x} F_{s,z} d\Omega \int_l N_i N_j dy$$

$$K_{zy}^{ij\tau s} = \tilde{C}_{13} \int_{\Omega} F_{\tau,z} F_s d\Omega \int_l N_i N_{j,y} dy$$

$$+ \tilde{C}_{55} \int_{\Omega} F_{\tau} F_{s,z} d\Omega \int_l N_{i,y} N_j dy$$

$$K_{zz}^{ij\tau s} = \tilde{C}_{11} \int_{\Omega} F_{\tau,z} F_{s,z} d\Omega \int_l N_i N_j dy$$

$$+ \tilde{C}_{66} \int_{\Omega} F_{\tau,x} F_{s,x} d\Omega \int_l N_i N_j dy$$

$$+ \tilde{C}_{55} \int_{\Omega} F_{\tau} F_s d\Omega \int_l N_{i,y} N_{j,y} dy$$

It should be noted that no assumptions on the approximation order have been made. It is therefore possible to obtain refined beam models without changing the formal expression of the nucleus components. This is the key-point of CUF which permits, with only nine FORTRAN statements, to implement any-order beam theories. The shear locking is corrected through the selective integration (see [1]). The line and surface integral computation is numerically performed by means of the Gauss method. The assembly procedure of the Lagrange-type elements is analogous to the one followed in the case of 2D elements. The procedure key-points are briefly listed:

1. The fundamental nucleus is exploited to compute the stiffness matrix of each cross-section element of a structural node. If an L4 element is considered, this matrix will have  $12 \times 12$  terms.
2. The stiffness matrix of the structural node is then assembled by considering all the cross-section elements and exploiting their connectivity.
3. The stiffness matrix of each beam element is computed and assembled in the global stiffness matrix.

The variationally coherent loadings vector is derived in the case of a generic concentrated load  $\mathbf{P}$ :

$$\mathbf{P} = \{ P_{u_x} \ P_{u_y} \ P_{u_z} \}^T \quad (18)$$

Any other loading condition can be similarly treated. The virtual work due to  $\mathbf{P}$  is:

$$\delta L_{ext} = \mathbf{P} \delta \mathbf{u}^T \quad (19)$$

The virtual variation of  $\mathbf{u}$  in the framework of CUF is:

$$\delta L_{ext} = F_\tau \mathbf{P} \delta \mathbf{u}_\tau^T \quad (20)$$

By introducing the nodal displacements and the shape functions, the previous equation becomes:

$$\delta L_{ext} = F_\tau N_i \mathbf{P} \delta \mathbf{q}_{\tau i}^T \quad (21)$$

This last equation permits us to identify the components of the nucleus which have to be loaded, that is, it leads to the proper assembling of the loading vector by detecting the displacement variables that have to be loaded.

The imposition of constraints can be carried out by considering each of the three degrees of freedom of cross-section element points independently. In other words, a constraint can be either imposed on the whole cross-section or on an arbitrary number of cross-section points.

## 4 Results and discussion

The proposed beam formulation is herein evaluated and compared with different models: classical beam theories, refined beam elements based on Taylor-type assumptions, and, in some cases, solid elements of the commercial code MSC Nastran. MSC Nastran models are based on HEX8 elements having approximatively a unitary aspect ratio. Various homogeneous cross-section geometries made of isotropic materials are analyzed. The material data is: the Young modulus,  $E$ , is equal to 75 [GPa]; the Poisson ratio,  $\nu$ , is equal to 0.33. Particular attention is given to problems that show the capability of the present beam element to deal with localized boundary conditions over the cross section as well as with plate/shell-like analyses. All the graphic results are opportunely scaled.

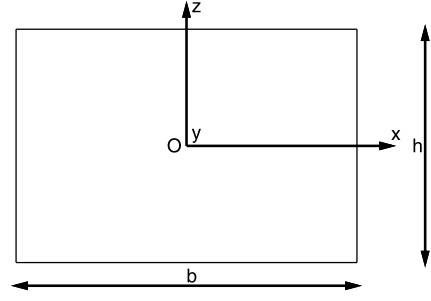


Fig. 4 Rectangular cross-section

Table 4 Effect of the number of elements on  $u_z$  for different beam models.  $L/h = 100$ . Compact square cross-section

No. Elem.	5	10	40
$u_z \times 10^2$ [m], $u_{z_b} \times 10^2 = -1.333$ [m]			
EBBM	-1.333	-1.333	-1.333
TBM	-1.333	-1.333	-1.333
$N = 1$	-1.333	-1.333	-1.333
$N = 2$	-1.314	-1.324	-1.331
1 L4	-1.107	-1.111	-1.115
1 L9	-1.314	-1.324	-1.331

### 4.1 Square and rectangular cross-sections

A cantilevered beam is used for the preliminary assessment of the present beam model. The geometry of the cross-section is shown in Fig. 4. The height of the cross-section,  $h$ , is 0.2 [m], with  $b$  as high as  $h$ . Two slenderness ratios,  $L/h$ , are considered: 100 and 10. Slender and moderately short beams are considered in order to highlight the importance of refined models in case of short structures. A point load,  $F_z$ , is applied at  $[0, L, 0]$ . The magnitude of  $F_z$  is equal to  $-50$  [N].

The loaded point vertical displacement,  $u_z$ , is evaluated. The Euler-Bernoulli theory is used for comparison purposes,  $u_{z_b} = \frac{F_z L^3}{3ET}$ , where  $I$  is the cross-section moment of inertia. Table 4 shows the displacement values for different meshes and beam models in the case of a slender beam ( $L/h = 100$ ). Classical theories, EBBM and TBM, are accounted for (2nd and 3rd rows). Results by Taylor-type linear and parabolic models,  $N = 1$  and  $N = 2$ , are reported in the 4th and 5th rows. Lagrange polynomial beam model results are shown in the last two rows. Four-point, L4, and nine-point, L9, cross-section elements are considered. Table 5 reports the results of a moderately

**Table 5** Effect of the number of elements on  $u_z$  for different beam models.  $L/h = 10$ . Compact square cross-section

No. Elem.	5	10	40
$u_z \times 10^5$ [m], $u_{z_b} \times 10^5 = -1.333$ [m]			
EBBM	-1.333	-1.333	-1.333
TBM	-1.343	-1.343	-1.343
$N = 1$	-1.343	-1.343	-1.343
$N = 2$	-1.320	-1.327	-1.330
$N = 3$	-1.322	-1.329	-1.332
$N = 4$	-1.323	-1.330	-1.333
1 L4	-1.112	-1.115	-1.116
1 L9	-1.320	-1.327	-1.329

**Table 6** Effect of the number of L4 elements on  $u_z$ .  $L/h = 100$ . Compact square cross-section

No. Elem.	1 L4	$2 \times 1$ L4	$1 \times 2$ L4	$2 \times 2$ L4
$u_z \times 10^2$ [m], $u_{z_b} \times 10^2 = -1.333$ [m]				
5	-1.107	-1.155	-1.222	-1.254
10	-1.111	-1.160	-1.229	-1.262
40	-1.115	-1.164	-1.234	-1.268

thick beam ( $L/h = 10$ ). Multiple L4 elements above the cross-section are used in Table 6. Each column refers to a different L4 discretization. The second column indicates the results obtained by using one L4, the third is related to the case of two L4 along the  $x$ -direction, the fourth to the case of two L4 along the  $z$ -direction, and the fifth to the case of two L4 elements along both cross-section directions. The results from all these analyses suggest the following considerations.

1. The use of an L9 permits us to obtain good accuracy. This element gives results which are equivalent to those of a Taylor-type parabolic,  $N = 2$ , model. This means that the cubic and quartic polynomial terms ( $s^2r$ ,  $sr^2$ , and  $s^2r^2$ ) do not play a very significant role in the considered problem, in fact, these terms are not considered in the Taylor case  $N = 2$ .
2. L4 have slower convergence rates than L9. However, the subdivision of the cross-section in more than one L4 is very effective.
3. The improvement given by the cross-section discretization in L4 elements is related to the total number of elements as well as their distribution

**Table 7** Role of the bilinear term and of the Poisson locking correction on  $u_z$ .  $L/h = 100$ . Compact square cross-section

Correction	Taylor bilinear	1 L4
$u_z \times 10^2$ [m], $u_{z_b} \times 10^2 = -1.333$ [m]		
Activated	-1.866	-1.868
Deactivated	-1.115	-1.115

above the cross-section. The refinement along the  $z$ -direction is more effective than the one along the  $x$ -direction when a  $F_z$  load is applied.

The L4 is characterized by the presence of a bilinear term in the displacement field expression. This term is responsible for the slow convergence rate. Table 7 presents the investigation on the role of the bilinear term together with the Poisson locking correction. Locking is corrected as in Carrera and Brischetto [4, 5]. The following Taylor-type model is used for comparison purposes:

$$\begin{aligned}
 u_x &= u_{x_1} + xu_{x_2} + zu_{x_3} + xzu_{x_5} \\
 u_y &= u_{y_1} + xu_{y_2} + zu_{y_3} + xzu_{y_5} \\
 u_z &= u_{z_1} + xu_{z_2} + zu_{z_3} + xzu_{z_5}
 \end{aligned} \tag{22}$$

This model has been obtained as in Carrera and Petrolo [7]. The following considerations arise from Table 7.

1. The L4 is equivalent to the bilinear Taylor expansion.
2. The Poisson locking correction corrupts the effectiveness of both models because of the presence of the bilinear term, but, at the same time, the bilinear term is not enough to eliminate the Poisson locking.
3. As a general remark it can be stated that a beam model based on a bilinear displacement field should not be used because of its convergence issues. Linear models (e.g. TBM or  $N = 1$ ) with a Poisson locking correction or at least a second-order model should be preferred to predict the bending behavior of a compact beam.

An equilateral triangular cross-section is now considered to conduct a further investigation on the role of the Poisson locking and its correction. Figure 5 shows the geometry of the triangle,  $b$  is equal to 1 [m] and  $L/b$  is as high as 20. A vertical force,  $F_z$ , is applied at the center point.  $F_z$  is equal to  $-30$  [N]. Two cross-section discretizations are used: 1 L3 and 2 L3. The

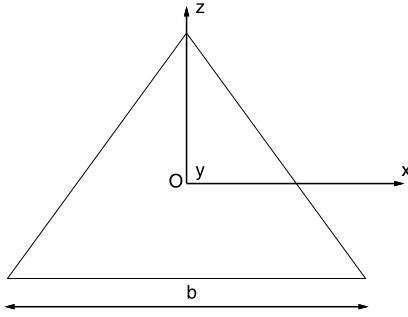


**Fig. 5** Triangular cross-section

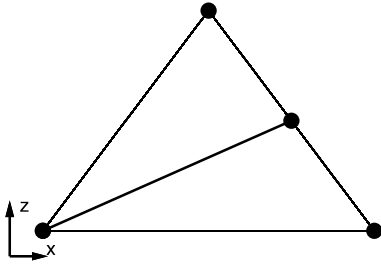


**Fig. 6** 2 L3 discretization of the triangular cross-section

**Table 8** Role of the Poisson locking correction on  $u_z$  in case of L3 elements. Compact triangular cross-section

Correction	1 L3	2 L3
$u_z \times 10^5$ [m], $u_{z_b} \times 10^5 = -5.912$ [m]		
Activated	-5.917	-7.300
Deactivated	-3.995	-4.567

latter one is shown in Fig. 6. Table 8 shows the vertical center point displacement values for both beam models and the effects of the Poisson locking correction. The result analysis suggests the following.

1. The Poisson locking correction is beneficial in the case of 1 L3 because a linear description of the cross-section displacement field is given. This confirms what has been previously mentioned about the role of the bilinear term.
2. The correction is detrimental in the case of 2 L3 because the displacement field is step-wise linear, therefore is overall higher than the first-order. However, more than 2 L3 elements are needed to nullify the Poisson locking. That explains why Poisson locking correction is not effective in L4 beam theories.

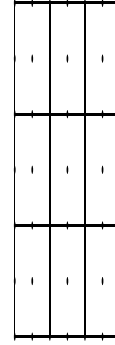


**Fig. 7** 3 × 3 L9 discretization of the rectangular cross-section

**Table 9** Displacement and stress values of the rectangular beam

SOLID	1 L9	3 × 3 L9	[x, y, z]
27000 DOF's	4941 DOF's	8967 DOF's	
$u_z \times 10^7$ [m]			
4.770	4.652	4.682	[0, L, -h/2]
$\sigma_{yy} \times 10^{-4}$ [Pa]			
1.292	1.296	1.291	[0, L/10, +h/2]
$\sigma_{yz} \times 10^{-2}$ [Pa]			
-6.168	-4.277	-6.086	[b/2, L/10, 0]

A rectangular cantilevered beam is now considered. The geometry of the cross-section is shown in Fig. 4. The height of the cross-section,  $h$ , is 0.1 [m], with  $b$  as high as  $h/4$  and  $L/h$  equal to six. A point load,  $F_z$ , is applied at [0, L, -h/2]. The magnitude of  $F_z$  is equal to -1 [N]. Two cross-section L9 distributions are adopted: a 1 L9 and a 3 × 3 L9. The latter is shown in Fig. 7. A 20 B4 mesh is used along the y-direction. Table 9 presents vertical displacements and stress values in different points; comparisons with a solid model are reported together with the computational cost of each model. Shear stress distributions above the cross-section are shown in Fig. 8. These results suggest the following.

1. A general good match is found between the present formulation and the solid model solution. A slight difference is observed in the vertical displacement because the loading point is considered where severe local effects undergo.
2. The cross-section discretization refinement is an effective method that leads to the 3D solid solution.

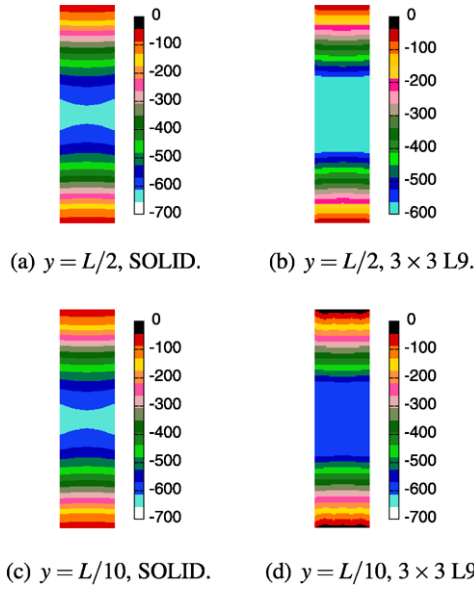


**Fig. 8**  $\sigma_{yz}$  distributions above the rectangular cross-section

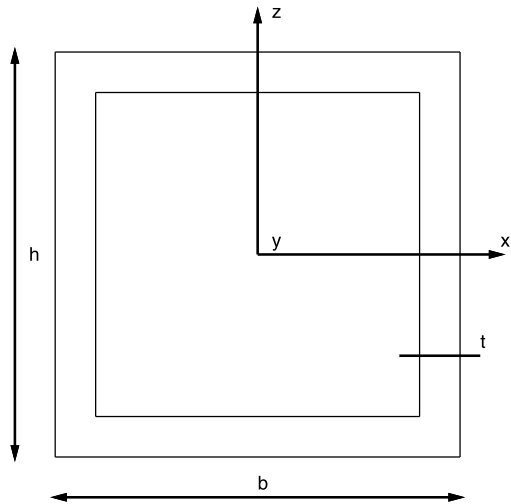


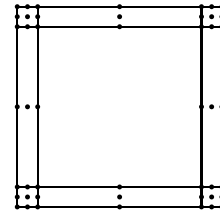
**Fig. 9** Hollow square cross-section

Shear stress distributions are particularly improved by the adoption of a refined cross-section model.

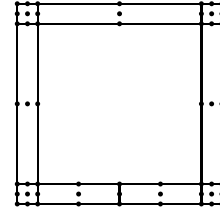
3. The present formulation requires significantly lower computational efforts than a solid model.

#### 4.2 Hollow cross-section

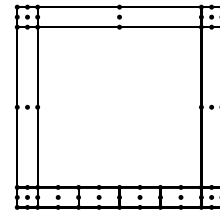
A hollow square cross-section is considered. Both ends are clamped. The cross-section geometry is shown in Fig. 9. The length-to-height ratio,  $L/h$ , is



(a) 8 L9



(b) 9 L9



(c) 11 L9

**Fig. 10** Cross-section element distributions for the hollow square beam

equal to 20. The height-to-thickness ratio,  $h/t$ , is equal to 10 with  $h$  as high as 1 [m]. A point load,  $F_z$ , is first considered and applied at  $[0, L/2, -h/2]$ . Its magnitude is equal to 1 [N]. Three cross-section discretizations have been used, as shown in Fig. 10. The 8 L9 distribution is symmetric, whereas the 9 L9, and the 11 L9 ones have been refined in the proximity of the loaded point. Table 10 shows the displacement,  $u_z$ , of the loaded point together with the indication of the number of degrees of freedom of each considered model. The first row shows the solid model result obtained by building a FE model in MSC Nastran. The increasing order Taylor-type models are considered in rows 2nd to 5th. The present Lagrange model results are shown in the last three rows. The following statements hold.

1. Refined beam theories allows us to obtain the solid model results.
2. The computational cost of the beam models is significantly smaller than the one requested by the 3D model.

**Table 10**  $u_z$  of the loaded point of the hollow square beam

	DOF's	$u_z \times 10^8$ [m]
SOLID	128952	1.374
Taylor		
EBBM	155	1.129
$N = 4$	1395	1.209
$N = 8$	4185	1.291
$N = 11$	7254	1.309
Lagrange		
8 L9, Fig. 2a	4464	1.277
9 L9, Fig. 2b	5022	1.308
11 L9, Fig. 2c	6138	1.326

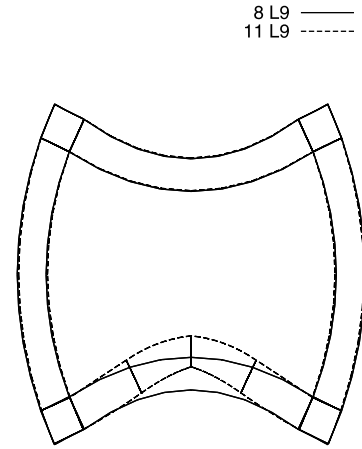
- An appropriate distribution of the L9 elements above the cross-section is effective in improving the accuracy of the solution. In other words, the local refinement of a beam model is possible and leads to the adaptation of the Lagrange point distribution to the given problem.
- Lagrange-based models are able to detect a more accurate solution than Taylor-based ones with reduced computational costs. This is due to the possibility of locally refining the beam model which is offered by the use of Lagrange polynomials, whereas a Taylor model uniformly spreads the refinement above the cross-section with no distinction between lowly and highly deformed zones.

A second load case is considered in order to better highlight the local refinement capabilities of the present beam formulation. Two point loadings ( $F_z = \pm 1$  [N]) are applied at  $[0, L/2, \mp h/2]$ . The adopted L9 distributions are those in Figs. 10a and 10c, that is, symmetric and asymmetric distributions are involved. The latter has a refined distribution just in the proximity of the bottom side load point. Table 11 shows the displacements of the two loaded point  $u_{z_{top}}$  and  $u_{z_{bot}}$ , respectively. Solid, as well as Taylor-type models, are used for comparison purposes. Figure 11 shows the deformed cross-section for each of the considered L9 element distributions. The following considerations are highlighted by this last example.

- Due to the symmetry of the geometry and of the load, the loaded points should be affected by the same vertical displacements (in magnitude). This result is obtained in all the considered cases unless the asymmetric L9 distribution is adopted. The lo-

**Table 11** Effect of the cross-section element distribution on the displacement of the loaded point. Hollow square beam

	DOF's	$u_{z_{top}} \times 10^9$ [m]	$u_{z_{bot}} \times 10^9$ [m]
SOLID	128952	-1.716	1.716
Taylor			
EBBM	155	0.0	0.0
$N = 4$	1395	-0.178	0.178
$N = 8$	4185	-1.046	1.046
$N = 11$	7254	-1.270	1.270
Lagrange			
8 L9, Fig. 2a	4464	-0.985	0.985
11 L9, Fig. 2c	6138	-0.972	1.456

**Fig. 11** Effect of the cross-section element distribution on the displacement field. Hollow square beam

- ally refined model leads to higher values for the displacements only in the proximity of the refinement.
- The solution improvement offered by Lagrange-based models is higher and computationally cheaper than the one offered by Taylor-type models.
- It has been shown that classical beam models, such as EBBM, are not capable of detecting the displacements of the loaded points at all.

#### 4.3 Open cross-sections

A cantilevered C-section beam is considered. The cross-section geometry is shown in Fig. 12. The length-to-height ratio,  $L/h$ , is equal to 20. The height-to-thickness ratio,  $h/t$ , is as high as 10 with  $h$  and  $b_2$

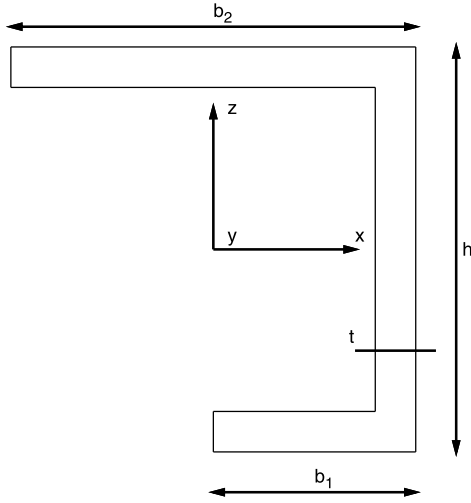
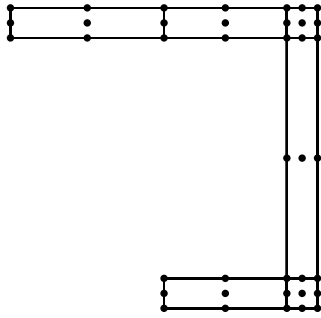
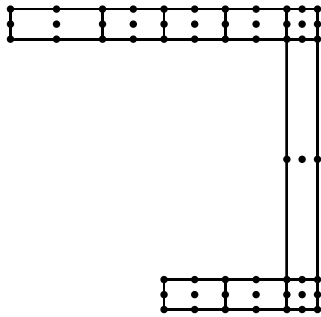


Fig. 12 C-section geometry



(a) 6 L9



(b) 9 L9

Fig. 13 Cross-section L9 distributions for the C-section beam

equal to 1 [m], and  $b_1$  as high as  $b_2/2$ . Two point loads are applied at  $[0, L, \pm 0.4]$ , and their magnitudes are as high as  $\mp 1$  [N]. Two L9 distributions are adopted and shown in Fig. 13. The 9 L9 distribution

Table 12 Vertical displacement,  $u_z$ , of the top loaded point. C-section beam

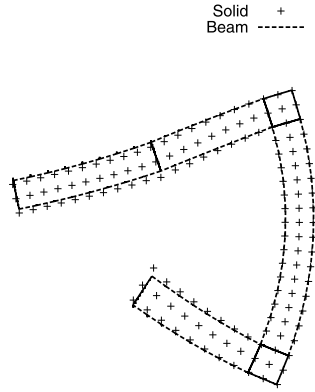
	DOF's	$u_z \times 10^8$ [m]
SOLID	84600	-3.067
Taylor		
EBBM	155	0.0
$N = 4$	1395	-0.245
$N = 8$	4185	-2.161
$N = 11$	7254	-2.565
Lagrange		
6 L9, Fig. 13a	3627	-2.930
9 L9, Fig. 13b	5301	-2.982

presents refinements in the proximity of the loading points. Table 12 shows the vertical displacement,  $u_z$ , of the point at  $[0, L, +0.4]$ . Solid models as well as Taylor-type beam models are considered together with the present beam formulation. Figure 14 show the free tip deformed cross-section for both the adopted L9 distributions. The solid model solution is reported as well. The following statements hold.

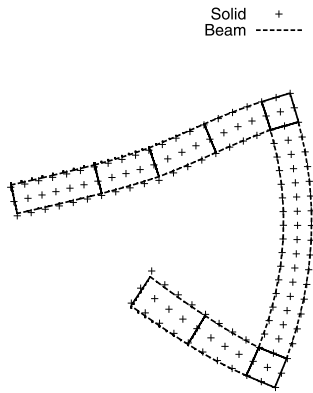
1. The 9 L9 model perfectly detects the solid solution with a significant reduction of the computational cost.
2. Taylor-type models require higher than eleventh-order expansions to match the solid model solution, consequently, the difference of computational cost between Taylor- and Lagrange-based beam models appears to be higher in the case of open, as opposed to closed cross-sections.
3. As seen previously, the classical model is totally inadequate to detect the displacement field of the considered structural problem.

A second loading condition is now considered: a flexural-torsional load is obtained by means of a point force applied at  $[b_1, L, -h/2]$ , its magnitude is equal to  $-1$  [N]. In this case, two  $L/h$  values are considered: 20 and 10. The L9 distribution shown in Fig. 13b is adopted. Displacement and stress values at different locations are presented in Tables 13 and 14, whereas stress distributions above the cross-section and the 3D deformed configuration are shown in Figs. 15, 16, and 17. These results suggest what follows.

1. The flexural-torsional behavior of a moderately short open cross-section beam is correctly predicted by the present formulation.



(a) 6 L9



(b) 9 L9

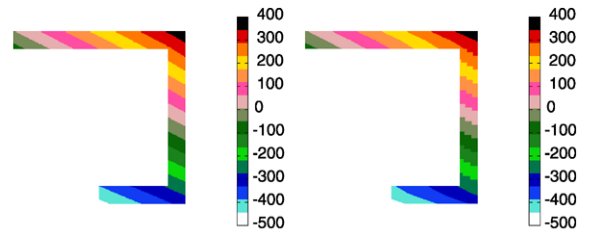
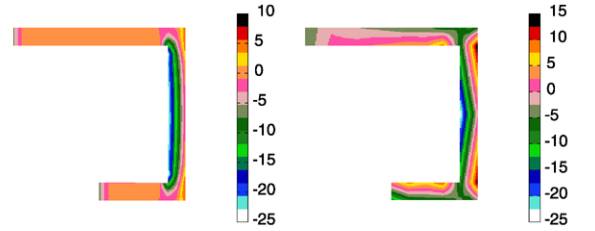
**Fig. 14** Deformed C-sections for different L9 distributions**Table 13** Displacements and stresses of the C-beam,  $L/h = 20$ 

SOLID	9 L9	$[x, y, z]$
84600 DOF's	5301 DOF's	
$u_z \times 10^6$ [m]		
-1.470	-1.462	$[-b_2/2, L, +h/2]$
$\sigma_{yy} \times 10^{-2}$ [Pa]		
3.880	3.976	$[b_1, L/10, +h/2]$
$\sigma_{xy} \times 10^{-2}$ [Pa]		
-1.636	-1.691	$[b_1, L, -h/2]$
$\sigma_{yz} \times 10^{-1}$ [Pa]		
-2.401	-2.348	$[0.4, L/10, 0]$

2. As far as stress distributions are considered, a good match with the solid model solution was found both for axial and shear components.

**Table 14** Displacements and stresses of the C-beam,  $L/h = 10$ 

SOLID	9 L9	$[x, y, z]$
84600 DOF's	5301 DOF's	
$u_z \times 10^7$ [m]		
-2.280	-2.272	$[-b_2/2, L, +h/2]$
$\sigma_{yy} \times 10^{-2}$ [Pa]		
2.030	2.055	$[b_1, L/10, +h/2]$
$\sigma_{yz} \times 10^{-2}$ [Pa]		
-4.345	-3.837	$[b_1, L, -h/2]$
$\sigma_{yz} \times 10^{-1}$ [Pa]		
-1.930	-1.863	$[0.4, L/10, 0]$

(a)  $\sigma_{yy}, y = L/10$ , SOLID.(b)  $\sigma_{yy}, y = L/10$ , 9 L9.(c)  $\sigma_{yz}, y = L/10$ , SOLID.(d)  $\sigma_{yz}, y = L/10$ , 9 L9.**Fig. 15** Stress distributions above the C cross-section,  $L/h = 20$ 

An open square cross-section is now considered. The cross-section geometry is shown in Fig. 18. The dimensions are the same of those seen in Sect. 4.2. Two opposite unit point loads,  $\pm F_x$ , are applied at  $[0, L, -0.45]$ . Three L9 distributions are adopted as shown in Fig. 19. Table 15 reports the horizontal displacement of the right-hand side loaded point which under-goes a positive horizontal force. A solid model is used to validate the results. The free-tip deformed cross-section is shown in Fig. 20. All the considered L9 distributions together with the solid model solution are reported. Figure 21 shows the 3D deformed configuration of the considered structure. The analysis of

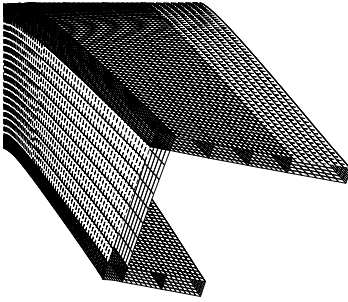
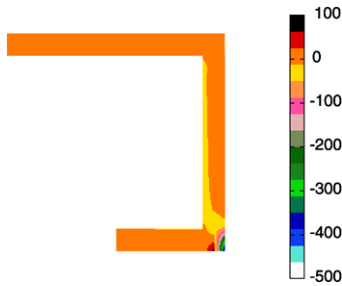
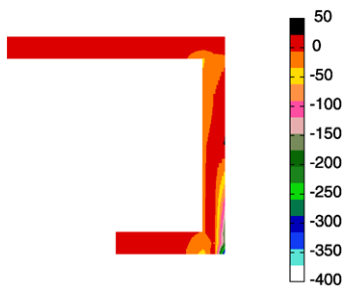


**Fig. 16** 3D deformed configuration of the C-section beam,  $L/h = 10$



(a)  $\sigma_{xy}, y = L, \text{SOLID}$ .



(b)  $\sigma_{xy}, y = L, 9 \text{ L9}$ .

**Fig. 17** Stress distributions above the C cross-section,  $L/h = 10$

the open hollow square beam highlights the following considerations.

1. The Lagrange-based beam model is able to deal with cut cross-sections.
2. This type of problem cannot be analyzed with Taylor-type beam models since the application of two opposite forces at the same point would imply null displacements.
3. The most appropriate refined L9 distribution does not necessarily lie in the proximity of load points.

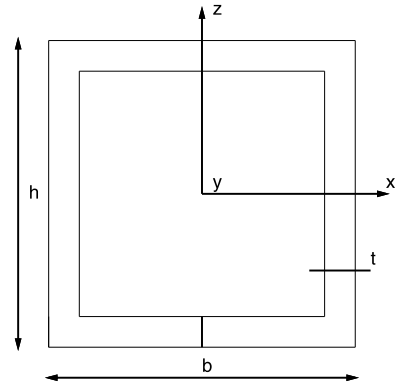
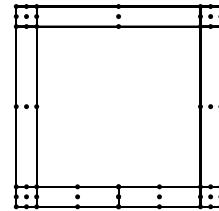
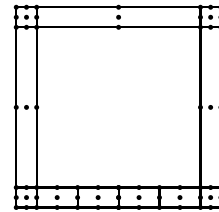


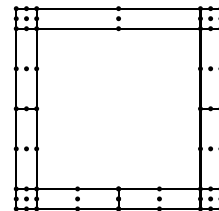
**Fig. 18** Open square cross-section



(a) 9 L9



(b) 11 L9<sup>a</sup>



(c) 11 L9<sup>b</sup>

**Fig. 19** Cross-section L9 distributions for the hollow square beam

In this case, the most effective refinement was the one placed above the vertical braces of the cross-section which undergo severe bending deformation.

**Table 15** Horizontal displacement,  $u_x$ , at  $[0, L, -h/2]$ . Open hollow square beam

	DOF's	$u_x \times 10^8$ [m]
SOLID	131400	5.292
9 L9, Fig. 20a	5301	4.884
11 L9 <sup>a</sup> , Fig. 20b	6417	4.888
11 L9 <sup>b</sup> , Fig. 20c	6417	5.116

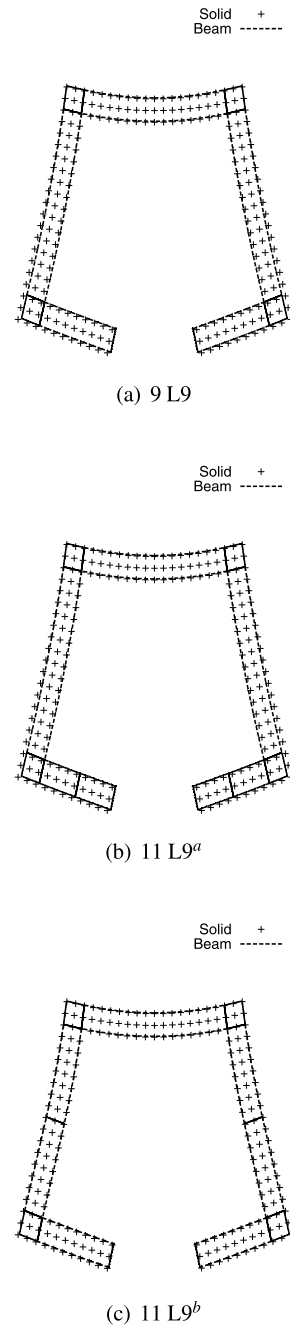
**Table 16** Vertical displacement,  $u_z$ , at  $[0, L/2, 0]$  of the rectangular cross-section beam with new constraints

	DOF's	$u_z \times 10^7$ [m]
SOLID	17271	-1.114
5 L9, Fig. 20a	3069	-0.959
10 L9 <sup>a</sup> , Fig. 20b	5859	-1.110

#### 4.4 Localized constraints over the cross-section

The present Lagrange-based beam formulation offers the important possibility of dealing with constraints that cannot be considered within classical and refined beam theories that make use of Taylor-type expansions. Beam model constraints usually act above the whole cross-section as shown in Fig. 22a (the beam longitudinal axis coincides with the  $y$ -axis). In the framework of the present approach, each of the three degrees of freedom of every Lagrange point of the beam can be constrained independently. This means that the cross-section can be partially constrained. Figure 22b shows a possible structural problem that can be faced where only the lateral edges of the cross-section are clamped. Figure 23 shows the  $x$ - $z$  view in the case of a rectangular cross-section.

A compact rectangular beam is first considered. The cross-section geometry and the cross-section constraint distribution is shown in Figs. 4 and 23, respectively. The length-to-height ratio,  $L/h$ , is equal to 100 with  $b/h$  as high as 10 and  $h$  equal to 0.01 [m]. A set of 21 unitary point loads is applied along the mid-span cross-section at  $z = h/2$  with constant  $x$ -steps starting from the edge of the cross-section. Two L9 distributions are adopted as shown in Fig. 24. Table 16 presents the center-point vertical displacement,  $u_z$ , of the considered beam models and that of solid elements. The deformed mid-span cross-section is shown in Fig. 25.

**Fig. 20** Deformed cross-sections of the hollow square beam

A circular arch cross-section beam is then analyzed to deal with a shell-like structure. The cross-section geometry and the constraint distribution is shown in Fig. 26. The length of the beam,  $L$ , is equal to 2 [m]. Outer,  $r_1$ , and inner,  $r_2$ , radii are equal to 1 and 0.9 [m], respectively. The angle of the arch,  $\theta$ , is equal

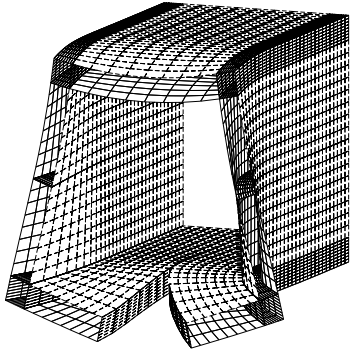


**Fig. 21** 3D deformed configuration of the hollow square beam. 11L9<sup>b</sup>

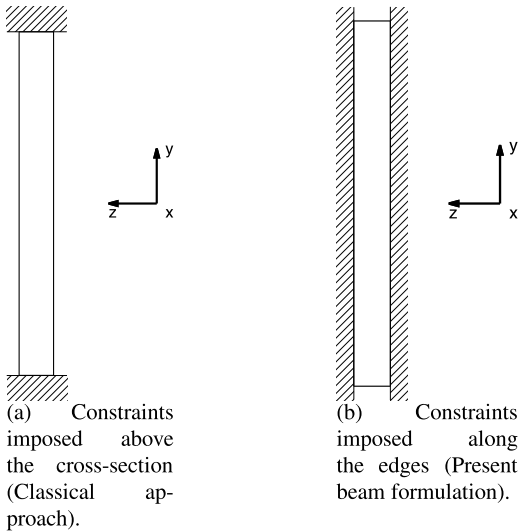


**Fig. 22** Comparison of classical and new constraint imposition approaches

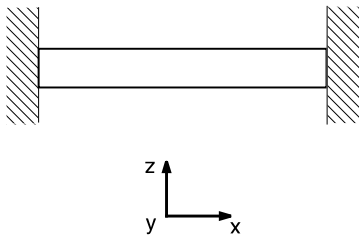
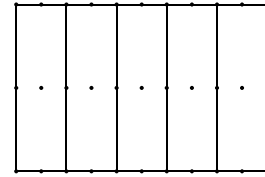
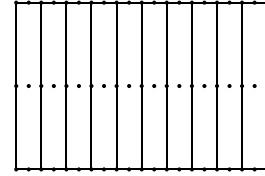


**Fig. 23** Boundary conditions above the rectangular cross-section

to  $\pi/4$  [rad]. Three unitary point loads are applied at  $y = 0$ ,  $y = L/2$ , and  $y = L$ . Each load acts along the radial direction (from the inner to the outer direc-



(a) 5 L9.



(b) 10 L9.

**Fig. 24** Rectangular cross-section L9 distributions

**Table 17** Vertical displacement,  $u_z$ , at the external surface of the arch cross-section beam,  $L = L/2$ ,  $\theta = \theta/2$

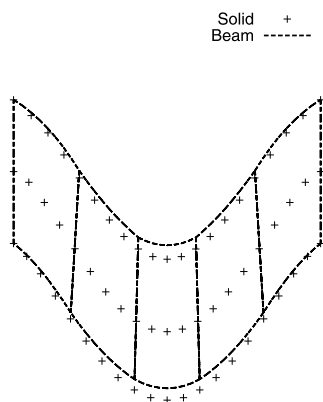
	DOF's	$u_z \times 10^{10}$ [m]
SOLID	43011	4.797
12 L9 <sup>a</sup> , Fig. 20b	6975	4.809

**Table 18** Displacement of the loaded point of the C-section beam

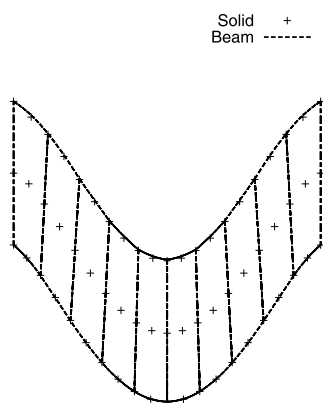
	DOF's	$u_z \times 10^8$ [m]
SOLID	84600	-3.759
13 L9 <sup>a</sup> , Fig. 20b	7533	-3.662

tion). The polar coordinates of the loading points are  $[r_2, \theta/2]$ . The L9 cross-section discretization is shown in Fig. 27. Table 17 shows the vertical displacement,  $u_z$ , of a point of the mid-span cross-section. The solid model solution is also reported. Figures 28 and 29 show the 2D and 3D deformed configurations, respectively.

The C-section beam is reconsidered to give a final assessment of this paper. The geometry is as in Sect. 4.3. Constraints are distributed along the bottom portions of the free-tip cross-sections as shown in Fig. 30. Two unitary point loads,  $F_z$ , are applied at  $[0, 0, 0.4]$  and  $[0, L, 0.4]$ , respectively. Both forces act along the negative direction. The L9 cross-section distribution is shown in Fig. 31. The loaded point vertical displacement,  $u_z$ , is reported in Table 18 and com-



(a) 5 L9.

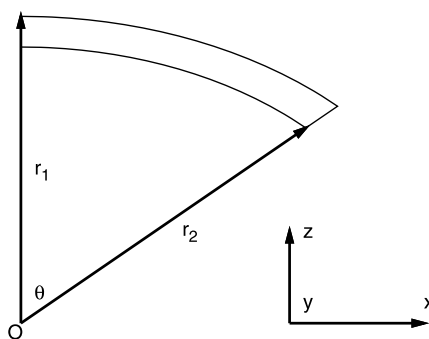


(b) 10 L9.

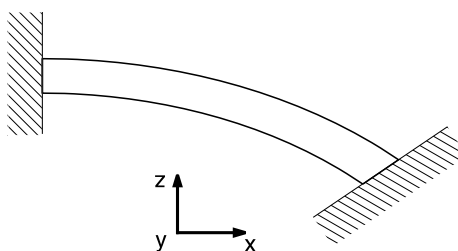
**Fig. 25** Mid-span deformed rectangular cross-section for different L9 distributions and comparison with a solid element model

pared with the value obtained from the solid model. Figures 32 and 33 show 2D and 3D deformed configurations, respectively. The following considerations can be made.

1. The results are in perfect agreement with those from solid models in all the considered cases.
2. The analysis of the rectangular cross-section beam has confirmed the possibility of dealing with partially constrained cross-section beams that is offered by the present formulation.
3. The constraints can be arbitrarily distributed in the 3D directions as shown by the analysis of the C-section beam.



(a) Geometry.



(b) Boundary conditions.

**Fig. 26** Circular arch cross-section

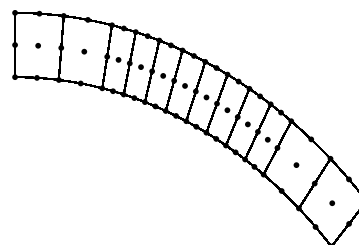


**Fig. 27** L9 distribution above the arch cross-section, 12 L9

4. The arch beam has shown the strength of the present beam model in dealing with beams that have shell-like characteristics. The local effects due to point loadings have also been detected.

## 5 Conclusions

This paper presents a novel beam formulation in the framework of the Carrera Unified Formulation (CUF). Lagrange polynomials have been used to define the displacement field above the cross-section of the beam. This choice has led to a beam formulation with sole displacement variables, that is, the unknowns

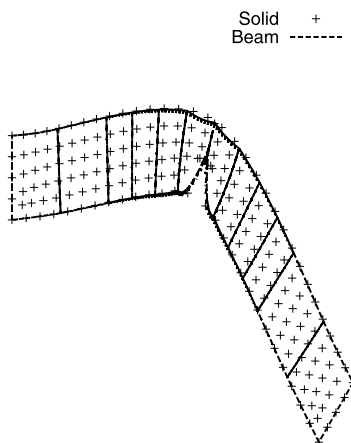


**Fig. 28** Free-tip deformed cross-section of the arch cross-section beam

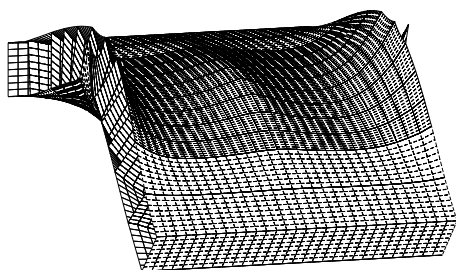


**Fig. 29** 3D deformed configuration of the arch cross-section beam

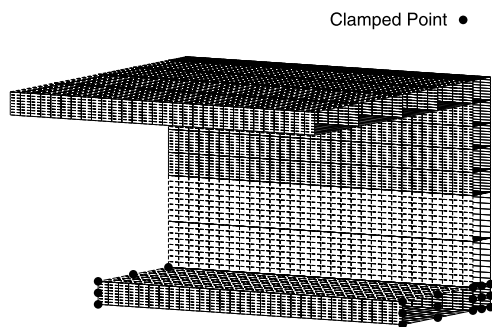


**Fig. 30** 3D clamped point distribution on the C-section beam

of the problem are the three translational displacement components of each Lagrange point above the cross-section. Three-point (L3), four-point (L4), and nine-point (L9) cross-section elements have been implemented. Multiple element distributions have been assembled as well. Several assessments have been considered: compact cross-sections, hollow closed and

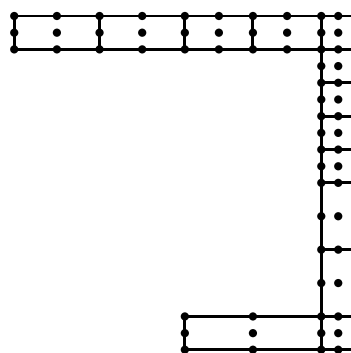


**Fig. 31** L9 distribution above the C-section, 13 L9

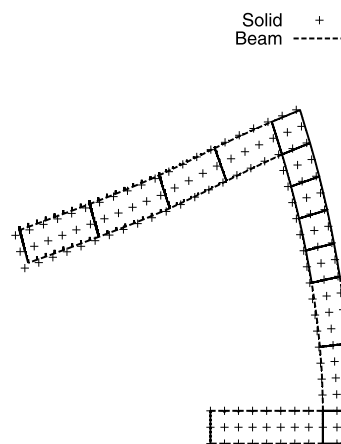


**Fig. 32** Deformed cross-section of the C-section beam.  $y = L$

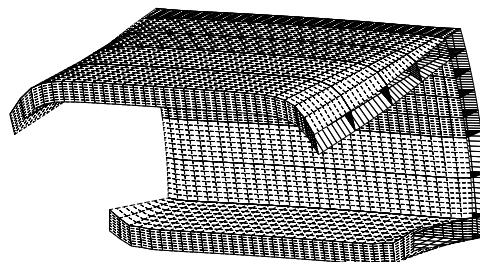


**Fig. 33** 3D deformed configuration of the C-section beam

open beams, and shell-like structures. Point loads have been applied. Taylor-type beam and solid models have been exploited for comparison purposes.

The construction of a refined beam model by means of the present Lagrange-based formulation has been achieved in two different ways.

1. By increasing the order of each Lagrange-type element (i.e. using a larger number of interpolation points per element).
2. By discretizing the cross-section and by using beam elements in sub-domains. This last option offers the possibility of adapting the element distribution to the considered problem with a consequent optimization of the computational cost.

The local refinement plays a fundamental role in dealing with point loads in the presence of open thin-walled cross-sections. In these cases, the Lagrange-based formulation has shown enhanced capabilities compared to the Taylor-based modeling. Other important capabilities of the present formulation are the following.

1. The Poisson locking correction is needed only in the case of single L3 elements. The assembly of two L3 or the use of L4 could make the correction detrimental.
2. The classical beam constraining approach has been overcome since a 3D distribution of the boundary conditions is possible. This implies the possibility of dealing with partially constrained cross-section beams, that is, the possibility of considering boundary conditions which are obtainable by means of plate/shell and solid models only.

The following considerations arise from the comparison with solid element models.

1. The results comply with all the assessed problems.
2. 3D solutions are obtained by model refining.
3. The computational cost of the present beam formulation is considerably lower than those incurred for 3D models.

The presence of only translational degrees of freedom appears to be attractive in the future perspective of the implementation of geometrically non-linear problems. The extension to the layer-wise analysis of composite structures could also be considered.

**Acknowledgements** The financial support from the Regione Piemonte project MICRO COST is gratefully acknowledged.

## References

1. Bathe K (1996) Finite element procedure. Prentice Hall, New York
2. Carrera E (2002) Theories and finite elements for multilayered, anisotropic, composite plates and shells. *Arch Comput Methods Eng* 9(2):87–140
3. Carrera E (2003) Theories and finite elements for multilayered plates and shells: a unified compact formulation with numerical assessment and benchmarking. *Arch Comput Methods Eng* 10(3):216–296
4. Carrera E, Brischetto S (2008) Analysis of thickness locking in classical, refined and mixed multilayered plate theories. *Compos Struct* 82(4):549–562
5. Carrera E, Brischetto S (2008) Analysis of thickness locking in classical, refined and mixed theories for layered shells. *Compos Struct* 85(1):83–90
6. Carrera E, Giunta G (2010) Refined beam theories based on Carrera's unified formulation. *Int J Appl Mech* 2(1):117–143
7. Carrera E, Petrolo M (2011) On the effectiveness of higher-order terms in refined beam theories. *J Appl Mech* 78(2). doi:10.1115/1.4002207
8. Carrera E, Giunta G, Nali P, Petrolo M (2010) Refined beam elements with arbitrary cross-section geometries. *Comput Struct* 88(5–6):283–293. doi:10.1016/j.compstruc.2009.11.002
9. Carrera E, Petrolo M, Nali P (2011) Unified formulation applied to free vibrations finite element analysis of beams with arbitrary section. *Shock Vib* 18(3):485–502. doi:10.3233/SAV-2010-0528
10. Carrera E, Petrolo M, Varello A (2011) Advanced beam formulations for free vibration analysis of conventional and joined wings. *J Aerosp Eng*. doi:10.1061/(ASCE)AS.1943-5525.0000130
11. Carrera E, Petrolo M, Zappino E (2011) Performance of CUF approach to analyze the structural behavior of slender bodies. *J Struct Eng*. doi:10.1061/(ASCE)ST.1943-541X.0000402
12. Dinis P, Camotim D, Silvestre N (2006) GBT formulation to analyse the buckling behaviour of thin-walled members with arbitrarily 'branched' open cross-sections. *Thin-Walled Struct* 44:20–38
13. Eisenberger M (2003) An exact high order beam element. *Comput Struct* 81:147–152
14. El Fatmi R (2007) Non-uniform warping including the effects of torsion and shear forces. Part I: a general beam theory. *Int J Solids Struct* 44:5912–5929
15. El Fatmi R (2007) Non-uniform warping including the effects of torsion and shear forces. Part II: analytical and numerical applications. *Int J Solids Struct* 44:5930–5952
16. Euler L (1744) *De curvis elasticis*. Bousquet, Lausanne
17. Gruttmann F, Wagner W (2001) Shear correction factors in Timoshenko's beam theory for arbitrary shaped cross-sections. *Comput Mech* 27:199–207
18. Gruttmann F, Sauer R, Wagner W (1999) Shear stresses in prismatic beams with arbitrary cross-sections. *Int J Numer Methods Eng* 45:865–889
19. Jönsson J (1999) Distortional theory of thin-walled beams. *Thin-Walled Struct* 33:269–303
20. Kapania K, Raciti S (1989) Recent advances in analysis of laminated beams and plates, part I: shear effects and buckling. *AIAA J* 27(7):923–935
21. Kapania K, Raciti S (1989) Recent advances in analysis of laminated beams and plates, part II: vibrations and wave propagation. *AIAA J* 27(7):935–946

22. Novozhilov VV (1961) *Theory of elasticity*. Pergamon, Elmsford
23. Oñate E (2009) *Structural analysis with the finite element method: linear statics*, vol 1. Springer, Berlin
24. Petrolito J (1995) Stiffness analysis of beams using a higher-order theory. *Comput Struct* 55(1):33–39
25. Reddy JN (1997) On locking-free shear deformable beam finite elements. *Comput Methods Appl Mech Eng* 149:113–132
26. Reddy JN (2004) *Mechanics of laminated composite plates and shells. Theory and analysis*, 2nd edn. CRC Press, Boca Raton
27. Rendek S, Baláž I (2004) Distortion of thin-walled beams. *Thin-Walled Struct* 42:255–277
28. Saadé K, Espion B, Warzée G (2004) Non-uniform torsional behavior and stability of thin-walled elastic beams with arbitrary cross sections. *Thin-Walled Struct* 42:857–881
29. Silvestre N (2007) Generalised beam theory to analyse the buckling behaviour of circular cylindrical shells and tubes. *Thin-Walled Struct* 45:185–198
30. Timoshenko SP (1921) On the corrections for shear of the differential equation for transverse vibrations of prismatic bars. *Philos Mag* 41:744–746
31. Timoshenko SP (1922) On the transverse vibrations of bars of uniform cross section. *Philos Mag* 43:125–131
32. Tsai SW (1988) *Composites design*, 4th edn. Think Composites, Dayton
33. Vinayak RU, Prathap G, Naganarayana BP (1996) Beam elements based on a higher order theory—I. Formulation and analysis of performance. *Comput Struct* 58(4):775–789
34. Wagner W, Gruttmann F (2002) A displacement method for the analysis of flexural shear stresses in thin-walled isotropic composite beams. *Comput Struct* 80:1843–1851
35. Yu W, Hodges DH (2004) Elasticity solutions versus asymptotic sectional analysis of homogeneous, isotropic, prismatic beams. *J Appl Mech* 71:15–23
36. Yu W, Volovoi VV, Hodges DH, Hong X (2002) Validation of the variational asymptotic beam sectional analysis (VABS). *AIAA J* 40:2105–2113